Development of Semi-Real-Time Tsunami Monitoring and Calculation System on Ocean-Bottom Stations off the Kii Peninsula, Southwest Japan

AUTHORS

Takeshi Nakamura*
Research and Development Center
for Earthquake and Tsunami,
Japan Agency for Marine-Earth
Science and Technology

Toshitaka Baba
Department of Civil and
Environmental Engineering,
The University of Tokushima

ABSTRACT

We developed a semi-real-time calculation and data monitoring system that measures pressure perturbations at ocean-bottom pressure-gauge stations deployed off the Kii peninsula in southwest Japan in order to identify tsunami signals associated with earthquakes. The system automatically calculates geodetic deformations and tsunami propagation immediately after getting seismic source information on hypocenter, magnitude, and mechanism. The calculation results for transoceanic tsunamis can be available in approximately 20 s after getting source information to output waveform data by executing the optimized parallel calculation code on our computer server SGI UV2000 with a 32-core processor unit. The system also provides tide-removed and filtered waveform data at ocean-bottom stations, enabling the calculation results to be compared with actual tsunami arrivals. System operations began in July 2015 and have been applied to tsunami-genic earthquakes in the Pacific Ocean. The system is effective in identifying tsunami signals and automatically predicting tsunami propagation in offshore areas, which may be useful for further data analyses on tsunami propagation.

Keywords: seafloor observatory science, DONET, Tonankai earthquake, real-time analysis, early warning

Introduction

Ocean-bottom observatory systems provide powerful means to monitor geophysical phenomena in ocean areas, such as seismic activity, geodetic deformations, submarine eruptions and landslides, turbidity and bottom currents, tides, and tsunamis. Such observations develop our understanding of the dynamics of the Earth through the ocean. Systems have been installed at local to regional scales by marine nations such as Canada (Barnes et al., 2008; Barnes et al., 2011, 2013), Japan (Hamada, 1985; Eguchi et al., 1998; Momma et al., 1998; Hirata et al., 2002), Taiwan (Hsiao et al., 2014), the United States (Romanowicz et al., 2009; Fulton-Bennett, 2010), and also in Europe (Ageron et al., 2011; Favali et al., 2013; Monna et al., 2014). In 2011, JAMSTEC (Japan Agency for Marine–Earth Science and Technology) deployed 22 sets of submarine-cabled geophysical stations, namely DONET1 (Dense Oceanfloor Network System for Earthquakes and Tsunamis), in water depths of 1,900–4,400 m off the Kii Peninsula in southwest Japan (Kawaguchi et al., 2011; Kaneda et al., 2015; Kawaguchi et al., 2015). JAMSTEC also deployed 29 sets of stations, DONET2, in water depths of 1,100–3,600 m on the western side off the Kii peninsula in 2016. We refer to these ocean-bottom observatory systems, DONET1 and 2, as "DONET."

Figure 1 shows the location of the DONET stations. Each station has strong motion and broadband seis-mometers, hydrophones, differential and quartz pressure gauges, and thermometers. These stations are expected to contribute to advancing "seafloor observatory sciences" reviewed by Favali and Beranzoli (2006), by opening the way to directly observe and investigate geophysical phenomena in deep ocean areas via dense arrays equipped with multiple types of sensors. DONET1 data have enabled us to investigate detailed hypocenter distributions (Nakano et al., 2013; Nakano et al., 2015) and mechanisms (Nakano et al., 2014) of small earthquakes; spectral features and seismic amplifications (Hayashimoto & Hoshiba,

Location of geophysical stations around the trough area, off the Kii peninsula in southwest Japan. The inset map shows southwest Japan. Red and yellow diamonds indicate ocean-bottom stations installed in the first- (DONET1) and second-phase plan (DONET2). DONET1 and DONET2 started fully operational observations in 2011 and 2016, respectively. Purple circles indicate tide gauge stations operated by JMA (Japan Meteorological Agency), GSI (Geospatial Information Authority of Japan), and MLIT (Ministry of Land, Infrastructure, Transport and Tourism). Green line with triangles is the Nankai trough. Black lines represent submarine cables. (Color version of figures are available online at: http://www.ingentaconnect.com/content/mts/mtsj/2016/00000050/00000003.)
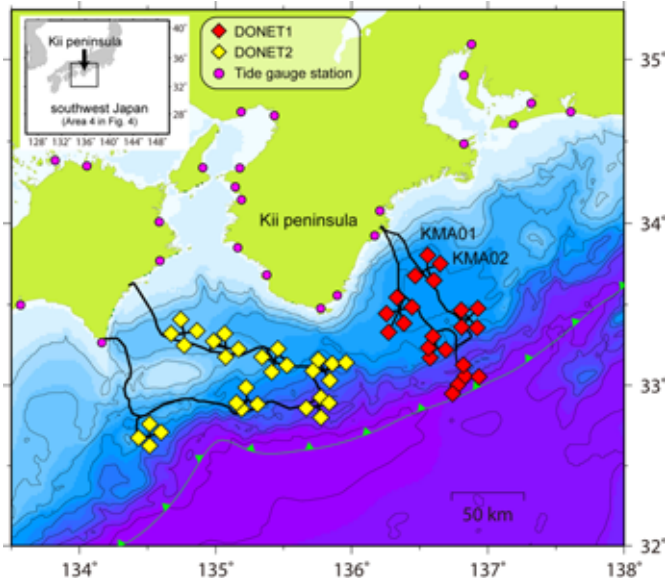
2013); spatial variations of amplifications and their simulation (Nakamura et al., 2014b); seismic signals of landslide events (Nakamura et al., 2014a), very low-frequency earthquakes (To et al., 2015) and infragravity waves (Tono et al., 2014); and signals of developed long-period motions (Nakamura et al., 2015) in ocean areas.

DONET seismic data are transferred to the Japan Meteorological Agency (JMA) in real time and are used to issue earthquake early warnings (Hoshiba et al., 2008; Kamigaichi et al., 2009). Monitoring and analyzing these seismic station data are very important, not only for basic geophysical research in deep ocean-bottom areas but also for earthquake disaster prevention/mitigation. DONET pressure sensor data are also expected to be useful for detecting tsunamis

(Rabinovich & Eblé, 2015) and for issuing tsunami warnings.

We recently developed a semi-real-time tsunami monitoring and calculation system to identify tsunami signals at DONET1 stations. The calculation tool is written in FORTRAN90 and Bourne Again SHell (BASH) and is easily installed and executed on Linux operating systems running on a server or personal home computer. The system calculates tsunami propagation and reads DONET1 data archived in our laboratory and produces graphical figures for data monitoring. In this paper, we describe the rapid, automatic calculation tool and show DONET1 data recorded by various types of sensors. We then compare calculation results with observations from tsunamigenic earthquakes in the Pacific Ocean. The calculation can even be

conducted on a personal home computer and provide results with graphical figures that help us understand the time variation and the spatial distribution of water heights. Finally, we explain our future plans for tsunami analyses using this system.

Fast Automatic Tsunami Calculation

We developed a tool to rapidly calculate geodetic deformation and tsunami propagation in ocean areas by implementing the code DC3D into parallel computations of deformation based on Okada (1992) that present the analytical equations of static deformation in a half-space and by developing a parallelized code for the tsunami propagation, referring to the numerical differential equations for the 2D linear long-wave approximation described in Satake (2002). To avoid time-consuming file I/O (input/output) operations, we combined the geodetic deformation and tsunami calculation parts by assuming the vertical component of geodetic deformation as the initial water height prior to tsunami propagation. We have confirmed that the waveforms calculated by our integrated code for a heterogeneous slip model are in agreement with waveforms presented by previous studies (e.g., Baba & Cummins, 2005). We implemented a hybrid MPI/OpenMP parallelization into the code to enable efficient parallel computation. Users can choose either the hybrid MPI/OpenMP or flat MPI approach when compiling the code in a simulation server, which offers flexibility to select the approach for efficient computations according to the compiler, computer architecture, and number of grids. In our case study, we employ the latter based on comparisons of

the computation times, including I/O, between these approaches. The code was optimized by paying careful attention to the order in which elements in array variables are accessed, avoiding subroutine calls in the innermost loop iteration, and avoiding the use of unnecessary conditional branches in loop iterations where processors spend much time. We have executed the optimized parallel code automatically, which is compiled by Intel Fortran Compiler, on a SGI UV2000 computer server (CPU: Intel Xeon E5-4627) since July 2015.

The calculation utilizes two types of input data. The first is source information for calculating geodetic deformation. We use the list of point source mechanisms from the Global Centroid Moment Tensor (Global CMT) solution (Dziewonski et al., 1981; Ekström et al., 2012), which estimates hypocenter, magnitude, and mechanism. The list used in the solution is updated through the Website within a few hours or days of large earthquake events. Our system automatically checks this list every 5 min and initiates calculations when new list entries are detected for large earthquakes (Figure 2). Since it is difficult to identify the main fault plane from a point source mechanism, our code calculates each geodetic displacement from two fault orientations simultaneously; i.e., one fault and its conjugate fault plane. In the calculation, we set the fault plane area by using the relationship between the size of the seismic moment M_0 (or moment magnitude M_w) and the static stress drop (Kanamori & Anderson, 1975) and assuming a stress drop of 3 MPa, which is a typical value obtained from crack models and source property analyses of large ($M \geq 6$) interplate earthquakes (Kanamori & Anderson, 1975). We

FIGURE 2

Analysis flow for calculating geodetic deformation and tsunami propagation.
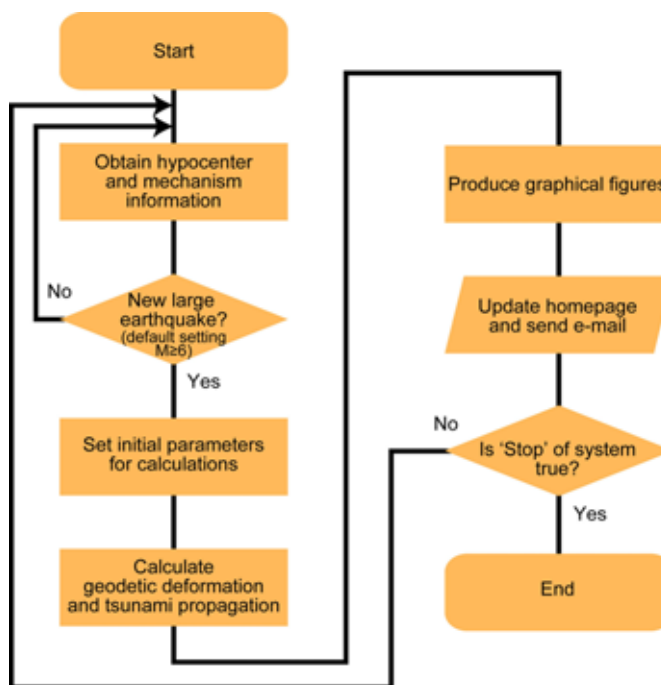
also use the duration of source rupture in the calculation, estimated via a scaling law between the seismic moment (or moment magnitude M_w) and the duration (e.g., Kikuchi, 2003). The equations for the fault plane area S (km^2) and duration T (s) are as follows:

$$\log S = M_W - 4 \qquad (1)$$

$$M_W = 2 \log T + 5. \qquad (2)$$

Assuming a homogeneous fault slip model in the fault plane as the source fault, we use the amount of slip D estimated from the fault size S, the size of the seismic moment M_0, and the rigidity μ at the source depth by using the equation of seismic moment $M_0 = \mu DS$ (Aki, 1966). For the rigidity, we use the value at the centroid depth of the Global CMT solution in the IASP91 earth model (Kennett & Engdahl,

1991). The ratio of fault lengths along strike and dip directions is assumed to be 2:1, which is typical for the fault size ratio (e.g., Geller, 1976). The methodology of setting parameters on source faults by means of a scaling law and of simultaneous calculations for two fault models has been proposed and implemented in recent studies (e.g., Inazu et al., 2014; Pulido et al., 2015), and a simulation software, TOAST (Tsunami Observation And Simulation Terminal), developed by a software company, gempa GmbH.

The second input source is bathymetric data for calculating tsunami propagation. The calculation area is divided into 32 subareas for parallel calculation by 32 processor cores of the server, providing subdivided bathymetric data with each core as input data (Figure 3). We prepare the subdivided data before executing calculations in order to avoid spending time inputting

FIGURE 3

Example of calculation area attributed to each CPU core. In the case of using the flat MPI parallelization of 32 cores, the total calculation area is divided into eight by four areas along the longitudinal and latitudinal directions, respectively, as indicated by green lines.
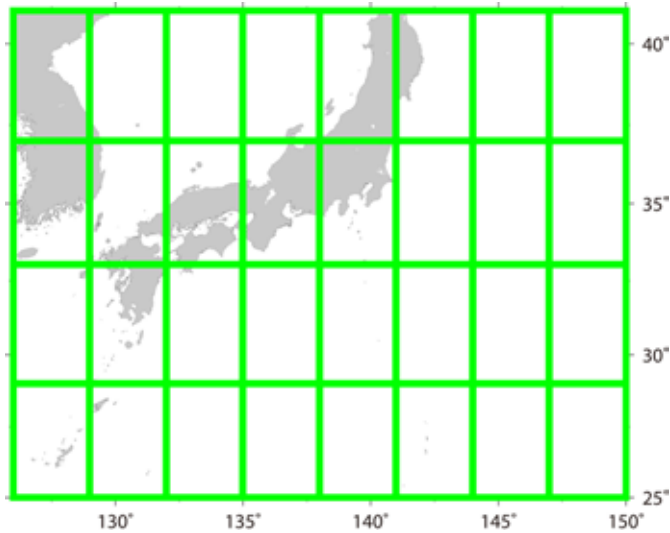
data for the whole area and subdividing the data during calculations.

In this system, we focus on geodetic deformation and tsunami propagation in the Pacific Ocean and their signals at DONET1 stations, located in southwest Japan (Figure 1). The calculation area depends on the epicentral location of an earthquake, namely, the entire area (Area 1), the northwest Pacific Ocean (Area 2), the ocean area around the Japanese islands (Area 3), or southwest Japan (Area 4). This categorization into four different areas is performed in order to efficiently calculate geodetic deformation and tsunami propagation from the source to DONET1 stations using a large grid size (or small number of grids) for a large area, such as calculations of the trans-Pacific tsunami, which usually dominates long-period components at stations when the signal comes from a large earthquake and can be calculated with a large grid size. For example, if the epicenter obtained from the Global CMT is located near southwest Japan, the system begins the calculation in Area 4 around southwest Japan and does not calculate the entire Pacific Ocean (Area 1). In the case of an epicenter near Chile, however, the system begins in Area 1 to calculate tsunami propagation from Chile to southwest Japan.

The system has an option to set the magnitude threshold in each area to begin calculations. By setting the threshold, for example, we can focus on only great earthquakes in Area 1 and avoid calculation of the trans-Pacific tsunami associated with the small to moderate (e.g., magnitude $M_w < 6$) far-field earthquakes, which usually result in low signal amplitudes at stations in Japan.

We present these four areas in Figure 4, and the coordinates for each area are shown in Table 1. We use bathymetric data from ETOPO2 and GEBCO for Areas 1–3 and Area 4, respectively. In calculations for Areas 1 and 2, we use decimated data of 7.5 and 5 arc-min from ETOPO2, respectively. We set the size of the time step

for each area based on a stability criterion that depends on spatial grid size and water depth. These values are summarized in Table 1.

After completing the calculations and producing graphical output of the results, the system uploads the figures to the server homepage on our institutional intranet and also forwards the results to the researchers by email. We show a flowchart from input to output for the calculations in Figure 2.

Tsunami Monitoring Using DONET1 Station Data

We developed a monitoring tool to identify tsunami signals from acoustic and seismic signals, as well as noise observed at DONET1 stations. The tool automatically generates tide-removed and noncausal bandpath-filtered waveform data from ocean-bottom pressure gauge data, and plots a daily graph of the waveforms within each 24-h period. We use theoretical tides calculated by NAOTIDEJ tide prediction software (Matsumoto et al., 2000). The period band of the filter is 100–7,200 s, which are typical dominant periods of observed tsunamis, and also 100–2,000 s, to detect small amplitude signals of short-period components such as microtsunamis (e.g., Hino et al., 2001). The tool also plots waveforms for differential pressure gauges and hydrophones, which are useful for estimating the arrival times of acoustic and seismic waves from earthquakes. Comparison between these plotted observations and the calculations verifies the accuracy and reliability of the calculation results and checks whether or not a predicted tsunami actually arrived at the stations.

Figure 5 shows an example of the plots at DONET1 station KMA01 for

FIGURE 4

Calculation area of geodetic deformation and tsunami propagation, selected from the four areas (Areas 1–4) based on earthquake epicenter.
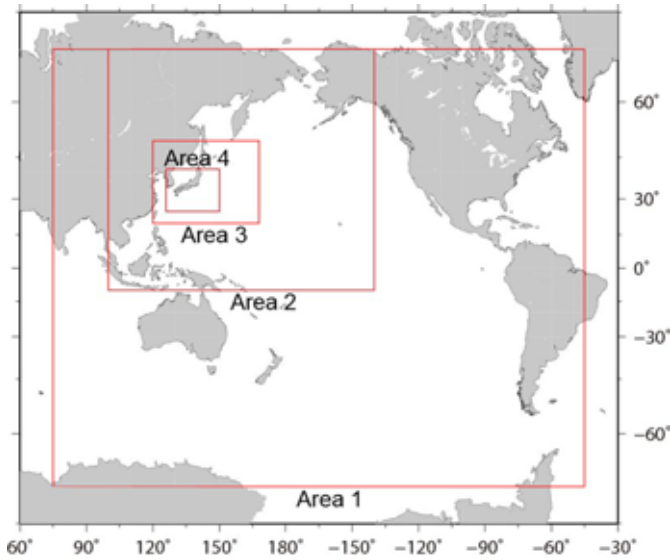
a distant earthquake and its associated tsunami. The station data are those for a large-magnitude 8.2 earthquake that occurred in central Chile at 22:54 UTC on September 16, 2015. We find short-period signals of seismic waves from the main shock in plots of the pressure gauge, differential pressure gauge, and hydrophone data at 23:15 UTC on September 16 (Figure 5a). We also find signals of the tsunami associated with the main shock in plots of the filtered waveform difference between pressure gauge and theoretical tide data at 22:00 UTC on September 17, 23 h after the origin time of the main shock (Figure 5b). Using the hydrostatic pressure equation to convert pressure to water height, the pressure gauge data after removing tide effects and filtering indicate a water height of 1.5 cm. The plot of the filtered waveform difference on September 18 shows the continued perturbations, indicating the long duration of tsunami propagation and successive arrivals at the DONET1 station (Figure 5c).

Results and Discussion

Our developed calculation tool automatically creates graphical figures for the spatial distribution of maximum tsunami height, as shown in Figure 6, which provides a visual map of areas with high-amplitude tsunami surges, such as those around the source, islands, and coasts. The tool also creates figures of the calculated tsunami waveforms to help identify tsunami signals from observation data. In this section, we examine the calculation results by comparing them with observations and then examine the computation time to obtain the results and limitations of our calculation.

Comparison of Calculations and Observations

Figure 7 shows three comparisons between the calculation results and observations. Figures 7a shows the results for station KMA01 for the Chilean earthquake (M_w 8.2) on September 16, 2015. Both of the waveforms are band-path-filtered within the period band 100–7,200 s. We simultaneously calculated tsunami propagation for two mechanisms, (strike 5°, dip 22°, rake 106°) and (strike 169°, dip 69°, rake 84°), in a grid size of 7.5 arc-min for Area 1 as shown in Figure 4 and Table 1. Since the DONET1 station is located far from the source, we did not find significant differences in the calculated waveforms between the two mechanisms, implying larger contributions from the propagation effects

TABLE 1

Focus areas and parameter data for calculation.

| Name	Longitude	Latitude	Grid Size	Total Number of Grid Cells	Total Number of Time Steps	Total Time Length	Bathymetric Data
Area 1	E75°-W45°	S70°-N70°	7.5 arc-min	1,921 × 1,121	7,714	108,000 s (30 h)	ETOPO2
Area 2	E100°-W140°	S10°-N70°	5 arc-min	1,441 × 961	8,064	100,800 s (28 h)	ETOPO2
Area 3	E120°-E168°	N20°-N50°	2 arc-min	1,441 × 901	8,640	43,200 s (12 h)	ETOPO2
Area 4	E126°-E150°	N25°-N41°	1 arc-min	1,441 × 961	7,200	21,600 s (6 h)	GEBCO

Observed waveform data at DONET1 station KMA01. Left (a), middle (b), and right (c) panels show data on September 16, 17, and 18, 2015, respectively. From the top, panels indicate the following: pressure gauge data (black line), theoretical tide data calculated by NAOTIDEJ (purple line), difference between pressure gauge and theoretical tide data (green line), bandpass-filtered difference within the period 100–2,000 s and 100–7,200 s (ocher line), water temperature from pressure gauge (blue line), water temperature from high-precision thermometer (red line), differential pressure (gray line), and hydrophone data (blue line).
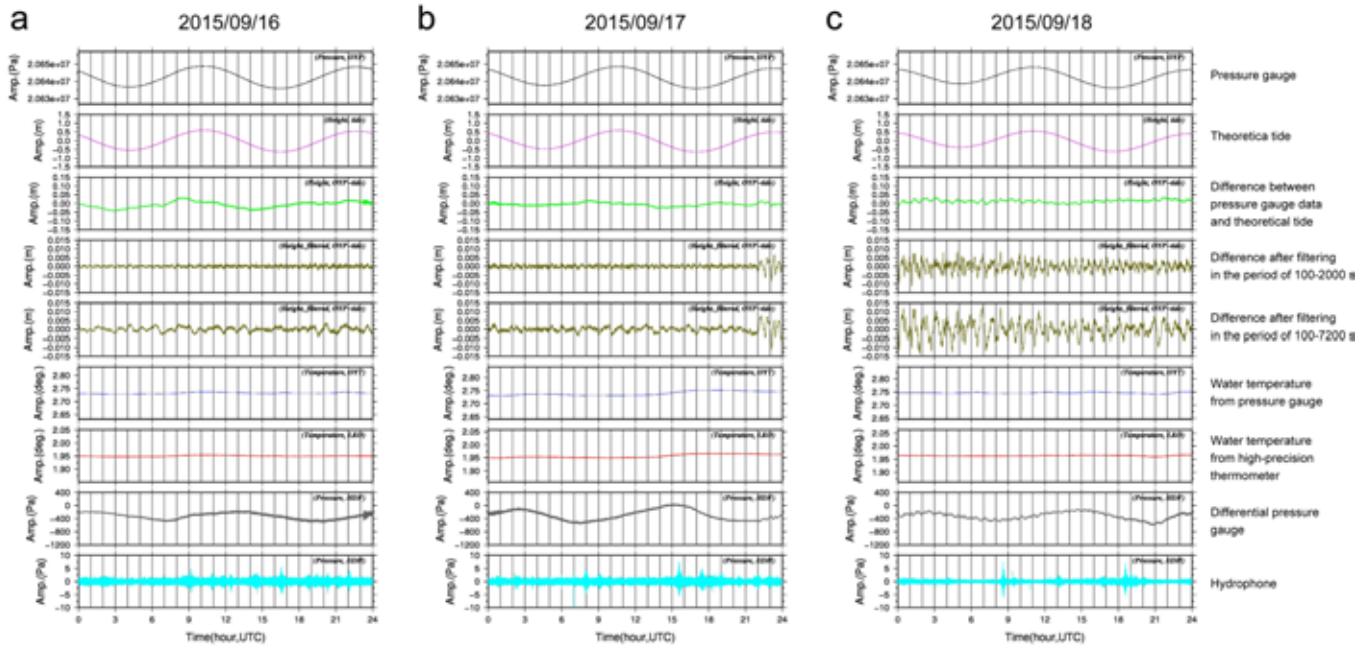
FIGURE 6

Distribution of maximum water height obtained from tsunami calculation of the 2015 central Chile earthquake.
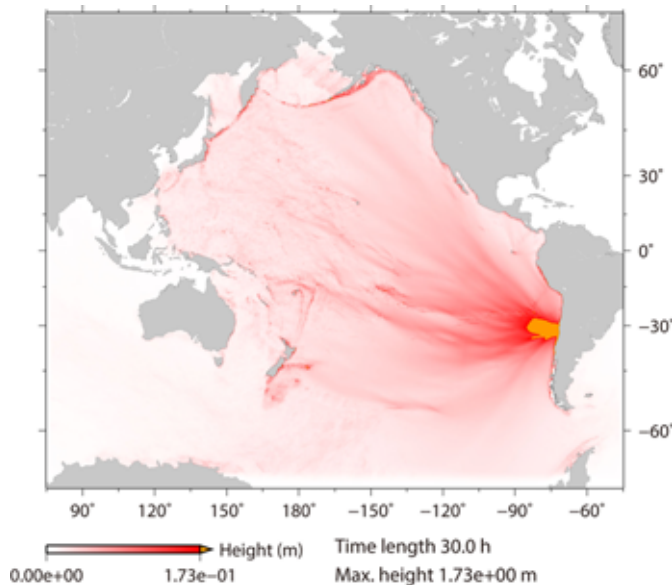

to the waveforms than from the source effect. Considering the great magnitude of the earthquake occurred in the subduction area, we show waveforms only for a low-angle thrust type mechanism (strike 5°, dip 22°, rake 106°) in Figure 7a.

The calculated waveforms represent earlier arrivals of the initial wave and larger amplitudes (including the coda) than those of the observations. Since we employ a very simple scheme for calculations (with assumptions such as a homogeneous fault slip model, geodetic deformation in a half-space, initial water height based on the vertical component of geodetic deformation, and 2D linear long-wave theory), many factors could contribute to the disparities in the arrivals and amplitudes. For the former disagreement, our assumption of the incompressibility of a seawater layer above a rigid ocean bottom

Calculated tsunami waveforms (red line) compared with observations (green line) at DONET1 stations. Observed waveforms were obtained by converting pressure data to water height using the hydrostatic equation. Upper and lower panels show nonfiltered and filtered waveforms, respectively. The original point for the horizontal axis is the origin time of earthquake. (a) Nonfiltered and filtered waveforms within the period 100–7,200 s at DONET1 station KMA01 for the 2015 central Chile earthquake. The synthetic waveforms show calculation results from a low-angle thrust type mechanism (strike 5°, dip 22°, rake 106°). (b) Nonfiltered and filtered waveforms within the period 100–2,000 s at DONET1 station KMA01 for the 2015 earthquake off the west shore of Kyushu, southwest Japan. The synthetic waveforms show calculation results from a strike-slip type mechanism (strike 191°, dip 83°, rake –173°). (c) Nonfiltered and filtered waveforms within the period 100–7,200 s at DONET1 station KMA02 for the 2011 Tohoku earthquake, northeast Japan. The synthetic waveforms show calculation results from a low-angle thrust type mechanism (strike 203°, dip 10°, rake 88°).
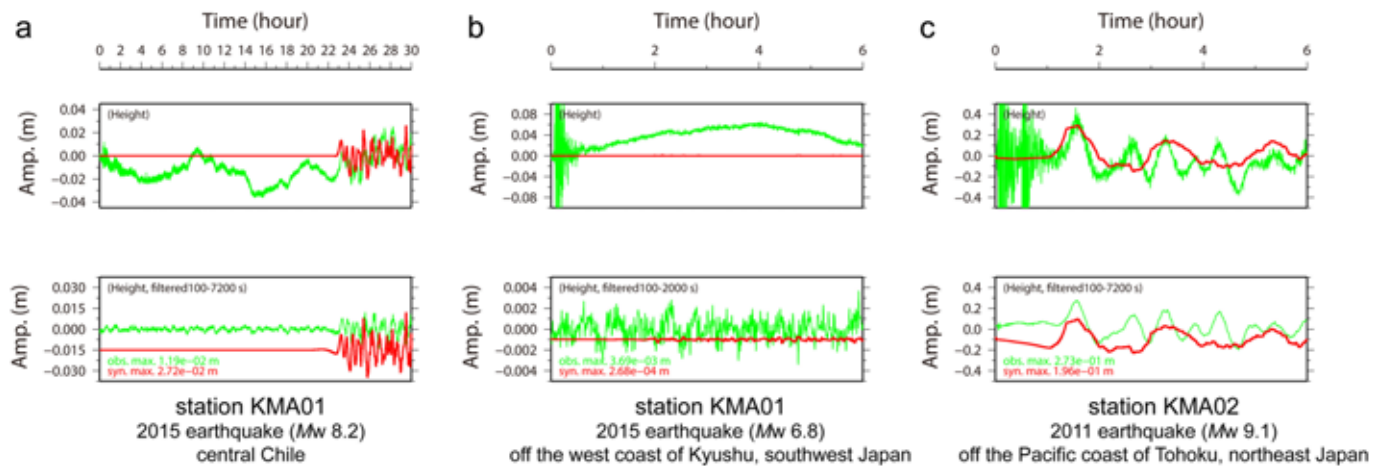
in the calculation may be the cause of earlier arrivals (9 min) within the period 100–7,200 s. A similar difference between calculated and observed tsunami arrivals has also been found at distant stations for other trans-Pacific tsunamis (e.g., Fujii & Satake, 2013). Such anomalies within the period band were explained by recent theoretical studies (Tsai et al., 2013; Watada et al., 2014), suggesting that seawater compressibility and elasticity of the solid earth can change the propagation speed of a tsunami as the main effects. Another possible cause is that, since in Area 1 we used a large grid size that can cause numerical dispersions and change waveforms, the dispersions may have caused a time difference between the observations and the affected synthetic waveforms. Note that here we measured the time difference not from the arrival times but from visual comparison of waveforms because

of the unclear onset of the first wave, which is contaminated with noise in the observation. For the latter disparity, the nondispersive nature of the linear long wave may be one possible cause of amplification. Since the linear long-wave theory does not consider the physical dispersion effect, simultaneous arrivals of many frequency components at stations may result in amplified waveforms. The homogeneous slip model in a fault plane, estimated from the seismic moment by applying a scaling law (e.g., Kikuchi, 2003), may also cause the latter disagreement as a consequence of uncertainties regarding the slip amount and its heterogeneous distribution. In either case, we suppose that the disagreement is not critical for identifying tsunami signals and rapidly providing preliminary calculation results.

The second comparison (Figure 7b) employs observations from station KMA01 for the 2015 earthquake

(M_w 6.8) that occurred off the west shore of Kyushu, southwest Japan, on November 13, 2015. The unfiltered data show clear, short-period seismic phases at around the origin time. However, tsunami signals are not detected in either the unfiltered or filtered (period 100–2,000 s) data. The synthetic waveforms show a maximum tsunami amplitude of 0.3 mm, which is of lower amplitude than the noise levels of the observations. Since this earthquake showed a strike-slip mechanism and was not of great magnitude, the tsunami signals from the source area are comparatively weak and may not propagate to the stations. As this example shows, our system is useful in verifying whether or not large tsunami events occur and propagate to the monitoring stations.

The third comparison (Figure 7c) employs observations for the 2011 Tohoku earthquake (M_w 9.1) that

occurred in northeastern Japan on March 11, 2011. Both of the waveforms are bandpath-filtered in the period 100–7,200 s. Since our automated analysis system began operation in July 2015, we plotted the observed and calculated data for the tsunami propagation associated with the 2011 earthquake in the nonautomated mode. Figure 7c shows data from station KMA02, since installation was incomplete at some stations (such as KMA01) at the time of this earthquake. The synthetic waveforms show filtered ones calculated for a low-angle thrust type mechanism (strike 203°, dip 10°, rake 88°).

The calculation results do not explain the observations in the waveforms of short-period components. This disagreement would primarily be caused by the source model, since the short-period component cannot be reproduced well by our calculation for near-field tsunamis assuming a simple source model of only a single fault plane with homogeneous slip. However, our rapid forward calculations reproduce the observed tsunami of long-period component to a first-order approximation and estimate approximate tsunami arrivals of the initial phase and the maximum amplitude.

Computation Time for Calculating Tsunami Propagation

Figure 8 shows the computation time required by our server for 53 large earthquakes that occurred since the system began operation in July 2015. We choose earthquakes of magnitude $M_w \geq 6$ in all areas for the purpose of statistical analysis using much of the data, although the calculated results do not reproduce the observations well for an M_w 6 earthquake (usually with fault length of 10 km) in Area 1 because the 7.5-arc-min grids are too coarse. Computation time includes

file input and output but excludes the time spent waiting for and getting the Global CMT solution and the production of graphical figures. The estimated computation times for transoceanic (Area 1) and other tsunamis (Areas 2–4) indicate a mode value of 18 s with a range of 17–21 s and 11 s with a range of 10–13 s, respectively.

This short computation time confirms that this system is useful for rapid forecasting of tsunami arrivals and amplitudes. This rapid calculation ability may also be useful for constructing databases of tsunami waveforms for anticipated fault models (e.g., Reymond et al., 2012), which can be time-consuming in many models when using nonoptimized calculation methods. Since our method employs 2D equations that do not utilize much of the computer memory, our rapid calculation can also be run on a home

personal computer. The total memory requirement for calculations is approximately 250 and 380 megabytes for Area 1 and Areas 2–4, respectively. For the 2015 Chile earthquake, the computation time was approximately 7 min when using a personal computer (4 cores, Intel 2.4 GHz Core 2 Quad Q6600 CPU).

Present Problems and Further Developments for Tsunami Monitoring and Calculations

At present, there are several aspects in which our rapid calculations may be improved. The first problem is that it may be difficult to calculate tsunami propagation for anomalous events, such as tsunami earthquakes with very slow rupture, CLVD (compensated linear vector dipole) earthquakes, or submarine landslides. We assume the vertical component of geodetic deformation estimated from a fault slip as the initial water height in the calculation; however, this simple assumption cannot be applied to such anomalous earthquakes. For tsunami earthquakes, prolonged ruptures do not generate approximately the same water height as the deformation expected in ocean-bottom areas. For CLVD earthquakes and submarine landslides, we cannot directly estimate mass movements, which cause the change in water height as the source of tsunami propagation, in ocean-bottom areas from the vertical component of geodetic deformation due to a shear dislocation of one fault plane.

The second problem is that the initial calculation conditions were based on source mechanisms from the Global CMT solution. Consequently, the calculation start time in our system depends on the time spent getting the source mechanisms. Since the Global CMT solution is presented after several

steps of data processing and quality checks, our calculations sometimes start one day after the occurrence of an earthquake. This may be improved by using alternative data sources in order to provide calculation results as soon as possible after an event.

Employing data assimilation method by using ocean-bottom pressure data is one of practical approaches to resolve the above two problems in the case of near-field events occurring around DONET stations. The tFISH algorithm by Tsushima et al. (2009) estimates initial water height from ocean-bottom data as tsunami source without estimating source mechanisms and fault models. The other data assimilation algorithm by Maeda et al. (2015) also estimates water height distribution that can be applied as initial condition for forward tsunami calculations. If we automatically analyze pressure data from DONET stations by integrating such data assimilation into our system and applying the resulting water height to our calculation, we may rapidly provide more accurate calculation results that can explain the observations, including those from anomalous near-field events. It may also be possible to forecast tsunami waveforms in coastal areas more rapidly than is possible in the present system. Our future work will focus on developing the present system by solving the problems associated with tsunami excitation source and their implementations.

Conclusion

We developed a semi-real-time calculation and data monitoring system that measures perturbations in ocean-bottom pressure for predicting and checking tsunami propagation associated with earthquakes. The system started operation in July 2015. We checked the accuracy and reliability of our automatic calculations by comparing them with monitoring data from ocean-bottom pressure-gauge stations deployed off the Kii peninsula in southwest Japan. The calculation results for transoceanic tsunamis can be available within approximately 20 s, from getting the source information to the output of waveform data, by executing optimized parallel code using our computer server SGI UV2000 with a 32-core CPU. The system is effective for identifying tsunami signals and predicting tsunami waveforms in offshore areas.

Acknowledgment

Corresponding Author:

Takeshi Nakamura*
Research and Development Center for Earthquake and Tsunami,
Japan Agency for Marine-Earth Science and Technology,
3173-25 Showa-machi, Kanazawa-ku, Yokohama 236-0001, Japan
* Now at National Research Institute for Earth Science and Disaster Resilience
Email: t_nakamura@bosai.go.jp

References

Ageron, M., Aguilar, J.A., Al Samaraj, I., Albert, A., Ameli, F., André, M., … Zúñiga, J. 2011. ANTARES: The first undersea neutrino telescope. Nucl Instr Methods Phys Res A. 656(1):11-38. http://dx.doi.org/10.1016/j.nima.2011.06.103.

Aki, K. 1966. Generation and propagation of G waves from the Niigata earthquake of June 14, 1964. Part 2. Estimation of earthquake moment, released energy and stress-strain drop from G wave spectrum. Inst Bull Earthquake Res. 44:73-88.

Baba, T., & Cummins, P.R. 2005. Contiguous rupture areas of two Nankai Trough earthquakes revealed by high-resolution tsunami waveform inversion. Geophys Res Lett. 32:L08305. http://dx.doi.org/10.1029/2004GL022320.

Barnes, C.R., Best, M.M.R., & Zielinski, A. 2008. The NEPTUNE Canada regional cabled ocean observatory—an overview of the progress of installation and the design of the science experiments. Sea Technol. 49(7):10-14.

Barnes, C.R., Best, M.M.R., Pautet, L., & Pirenne, B. 2011. Understanding Earth-ocean processes using real-time data from NEPTUNE, Canada's widely distributed sensor networks, northeast Pacific. Geosci Canada. 38(1):21-30.

Barnes, C.R., Best, M.M.R., Johnson, F.R., Pautet, L., & Pirenne, B. 2013. Challenges, benefits, and opportunities in installing and operating cabled ocean observatories: Perspectives from NEPTUNE Canada. IEEE J Oceanic Eng. 38(1):144-57. http://dx.doi.org/10.1109/UT.2011.5774134.

Dziewonski, A., Chou, T., & Woodhouse, J. 1981. Determination of earthquake source

parameters from waveform data for studies of global and regional seismicity. J Geophys Res. 86(B4):2825-52. http://dx.doi.org/10.1029/JB086iB04p02825.

Eguchi, T., Fujinawa, Y., Fujita, E., Iwasaki, S., Watabe, I., & Fujiwara, H. 1998. A real-time observation network of ocean-bottom-seismometers deployed at the Sagami trough subduction zone, central Japan. Mar Geophys Res. 20(2):73-94. http://dx.doi.org/10.1023/A:1004334021329.

Ekström, G., Nettles, M., & Dziewonski, A.M. 2012. The global CMT project 2004–2010: Centroid-moment tensors for 13,017 earthquakes. Phys Earth Planet In. 200–201:1-9. http://dx.doi.org/10.1016/j.pepi.2012.04.002.

Favali, P., Chierici, F., Marinaro, G., Giovanetti, G., Azzarone, A., Beranzoli, L., … Pavan, G. 2013. NEMO-SN1 Abyssal Cabled Observatory in the Western Ionian Sea. IEEE J Oceanic Eng. 38(2):358-74. http://dx.doi.org/10.1109/JOE.2012.2224536.

Favali, P., & Beranzoli, L. 2006. Seafloor observatory science: A review. Ann Geophys. 49(2/3):515-67. doi:10.4401/ag-3125.

Fujii, Y., & Satake, K. 2013. Slip distribution and seismic moment of the 2010 and 1960 Chilean earthquakes inferred from tsunami waveforms and coastal geodetic data. Pure Appl Geophys. 170(9):1493-509. http://dx.doi.org/10.1007/s00024-012-0524-2.

Fulton-Bennett, K. 2010. Selected engineering highlights at MBARI. Sea Technol. 51(1):22-4.

Geller, R.J. 1976. Scaling relations for earthquake source parameters and magnitudes. Bull Seismol Soc Am. 66(5):1501-23.

Hamada, N. 1985. T-waves recorded by ocean bottom seismographs off the south coast of Tokai area, central Honshu, Japan. J Phys Earth. 33(5):391-410. http://dx.doi.org/10.4294/jpe1952.33.391.

Hayashimoto, N., & Hoshiba, M. 2013. Examination of travel time correction and magnitude correction of Tonankai ocean bottom seismographs for Earthquake Early Warning. Quart J Seismol. 76(3/4):69-81. (in Japanese with English abstract)

Hino, R., Tanioka, Y., Kanazawa, T., Sakai, S., Nishino, M., & Suyehiro, K. 2001. Micro-tsunami from a local interplate earthquake detected by cabled offshore tsunami observation in northeastern Japan. Geophys Res Lett. 28(18):3533-36. http://dx.doi.org/10.1029/2001GL013297.

Hirata, K., Aoyagi, M., Mikada, H., Kawaguchi, K., Kaiho, Y., Iwase, R., … Fujiwara, N. 2002. Real-time geophysical measurements on the deep seafloor using submarine cable in the southern Kurile subduction zone. IEEE J Oceanic Eng. 27(2):170-81. http://dx.doi.org/10.1109/JOE.2002.1002471.

Hoshiba, M., Kamigaichi, O., Saito, M., Tsukada, S., & Hamada, N. 2008. Earthquake early warning starts nationwide in Japan. EOS Trans AGU. 89(8):73-4. http://dx.doi.org/10.1029/2008EO080001.

Hsiao, N.C., Lin, T.W., Hsu, S.K., Kuo, K.W., Shin, T.C., & Leu, P.L. 2014. Improvement of earthquake locations with the Marine Cable Hosted Observatory (MACHO) offshore NE Taiwan. Mar Geophys Res. 35(3):327-36. http://dx.doi.org/10.1007/s11001-013-9207-3.

Inazu, D., Saito, T., Kumagai, H., Pulido, N., & Fukuyama, E. 2014. Real-time tsunami simulation and visualization system using rapid CMT solutions in Southeast Asia. Japan Geoscience Union Meeting, 2014. HDS27-11, Yokohama, Japan.

Kamigaichi, O., Saito, M., Doi, K., Matsumori, T., Tsukada, S., Takeda, K., … Watanabe, Y. 2009. Earthquake early warning in Japan: Warning the general public and future prospects. Seismol Res Lett. 80(5):717-26. http://dx.doi.org/10.1785/gssrl.80.5.717.

Kanamori, H., & Anderson, D.L. 1975. Theoretical basis of some empirical relations in seismology. Bull Seismol Soc Am. 65(5):1073-95.

Kaneda, Y., Kawaguchi, K., Araki, E., Matsumoto, H., Nakamura, T., Kamiya, S., … Takahashi, N. 2015. Development and application of an advanced ocean floor network system for megathrust earthquakes and tsunamis. In: Seafloor Observatories, eds. Favali, P., Berazoli, L., & De Santis, A., 643-62. Chichester, UK: Springer Praxis Books. http://dx.doi.org/10.1007/978-3-642-11374-1_25.

Kawaguchi, K., Kaneko, S., Nishida, T., & Komine, T. 2015. Construction of the DONET real-time seafloor observatory for earthquakes and tsunami monitoring. In: Seafloor Observatories, eds. Favali, P., Berazoli, L., & De Santis, A., 211-28. Chichester, UK: Springer Praxis Books. http://dx.doi.org/10.1007/978-3-642-11374-1_10. (in Japanese with English abstract)

Kawaguchi, K., Araki, E., & Kaneda, Y. 2011. Establishment of a method for real-time and long-term seafloor monitoring. J Adv Mar Sci Tech Soc. 17(2):125-35.

Kennett, B.L.N., & Engdahl, E.R. 1991. Traveltimes for global earthquake location and phase identification. Geophys J Int. 105(2):429-65. http://dx.doi.org/10.1111/j.1365-246X.1991.tb06724.x.

Kikuchi, M. 2003. Realtime seismology. Tokyo: University Tokyo Press. 222 pp. (in Japanese)

Maeda, T., Obara, K., Shinohara, M., Kanazawa, T., & Uehira, K. 2015. Successive estimation of a tsunami wave-field without earthquake source data: A data assimilation approach toward real-time tsunami forecasting. Geophys Res Lett. 42:7923-32. http://dx.doi.org/10.1002/2015GL065588.

Matsumoto, K., Takanezawa, T., & Ooe, M. 2000. Ocean tide models developed by assimilating TOPEX/POSEIDON altimeter data into hydrodynamical model: A global model and a regional model around Japan. J Oceanogr. 56(5):567-81. http://dx.doi.org/10.1023/A:1011157212596.

Momma, H., Iwase, R., Mitsuzawa, K., Kaiho, Y., & Fujiwara, Y. 1998. Preliminary results of a three-year continuous observation by a deep seafloor observatory in Sagami Bay, central Japan. Phys Earth Planet In. 108(4):

263-74. http://dx.doi.org/10.1016/S0031-9201(98)00107-1.

Monna, S., Falcone, G., Beranzoli, L., Chierici, G., De Caro, M., De Santis, A., … Favali, P. 2014. Underwater geophysical monitoring for European Multidisciplinary Seafloor and water column Observatories. J Mar Syst. 130:12-30. http://dx.doi.org/10.1016/j.jmarsys.2013.09.010.

Nakamura, T., Takenaka, H., Okamoto, T., & Kaneda, Y. 2014a. Seismic wavefields in the deep seafloor area from a submarine landslide source. Pure Appl Geophys. 171(7):1153-67. http://dx.doi.org/10.1007/s00024-013-0717-3.

Nakamura, T., Nakano, M., Hayashimoto, N., Takahashi, N., Takenaka, H., Okamoto, T., … Kaneda, Y. 2014b. Anomalously large seismic amplifications in the seafloor area off the Kii peninsula. Mar Geophys Res. 35(3):255-70, http://dx.doi.org/10.1007/s11001-014-9211-2.

Nakamura, T., Takenaka, H., Okamoto, T., Ohori, M., & Tsuboi, S. 2015. Long-period ocean-bottom motions in the source areas of large subduction earthquakes. Sci Rep. 5:16648. http://dx.doi.org/10.1038/srep16648.

Nakano, M., Nakamura, T., Kamiya, S., Ohori, M., & Kaneda, Y. 2013. Intensive seismic activity around the Nankai trough revealed by DONET ocean-floor seismic observations. Earth Planets Space. 65(1):5-15. http://dx.doi.org/10.5047/eps.2012.05.013.

Nakano, M., Nakamura, T., Kamiya, S., & Kaneda, Y. 2014. Seismic activity beneath the Nankai trough revealed by DONET ocean-bottom observations. Mar Geophys Res. 35(3):271-84. http://dx.doi.org/10.1007/s11001-013-9195-3.

Nakano, M., Nakamura, T., & Kaneda, Y. 2015. Hypocenters in the Nankai trough determined by using data from both ocean-bottom and land seismic networks and a 3D velocity structure model: Implications for seismotectonic activity. Bull Seismol Soc Am. 105(3):1594-605. http://dx.doi.org/10.1785/0120140309.

Okada, Y. 1992. Internal deformation due to shear and tensile faults in a half-space. Bull Seismol Soc Am. 82(2):1018-40.

Pulido, N., Inazu, D., Saito, T., Senda, J., Fukuyama, E., & Kumagai, H. 2015. Real time earthquake information and tsunami estimation system for Indonesia, Philippines and Chile regions. Japan Geoscience Union Meeting, 2015. HDS27-P03, Makuhari, Japan.

Rabinovich, A.B., & Eblé, M.C. 2015. Deep-Ocean Measurements of Tsunami Waves. Pure Appl Geophys. 172(12):3281-312. http://dx.doi.org/10.1007/s00024-015-1058-1.

Reymond, D., Okal, E.A., Hébert, H., & Bourdet, M. 2012. Rapid forecast of tsunami wave heights from a database of pre-computed simulations, and application during the 2011 Tohoku tsunami in French Polynesia. Geophys Res Lett. 39:L11603. http://dx.doi.org/10.1029/2012GL051640.

Romanowicz, B., McGill, P., Neuhauser, D., & Dolenc, D. 2009. Acquiring real time data from the broadband ocean bottom seismic observatory at Monterey Bay (MOBB). Seismol Res Lett. 80(2):197-202. http://dx.doi.org/10.1785/gssrl.80.2.197.

Satake, K. 2002. Tsunamis. In: International Handbook of Earthquake and Engineering Seismology, eds. Lee, W.H.K., Kanamori, H., Jennings, P.C., & Kisslinger, C., 437-51. Amsterdam: Academic Press. http://dx.doi.org/10.1016/S0074-6142(02)80231-5.

To, A., Obana, K., Sugioka, H., Araki, E., Takahashi, N., & Fukao, Y. Small size very low frequency earthquakes in the Nankai accretionary prism, following the 2011 Tohoku-Oki earthquake. Phys Earth Planet In. 245:40-51. http://dx.doi.org/10.1016/j.pepi.2015.04.007.

Tono, Y., Nishida, K., Fukao, Y., To, A., & Takahashi, N. 2014. Source characteristics of ocean infragravity waves in the Philippine Sea: Analysis of 3-year continuous network records of seafloor motion and pressure. Earth Planets Space. 66(1):99. http://dx.doi.org/10.1186/1880-5981-66-99.

Tsai, V.C., Ampuero, J.-P., Kanamori, H., & Stevenson, D.J. 2013. Estimating the effect of Earth elasticity and variable water density on tsunami speeds. Geophys Res Lett. 40:492-6. http://dx.doi.org/10.1002/grl.50147.

Tsushima, H., Hino, R., Fujimoto, H., Tanioka, Y., & Imamura, F. 2009. Near-field tsunami forecasting from cabled ocean bottom pressure data. J Geophys Res. 114:B06309. http://dx.doi.org/10.1029/2008JB005988.

Watada, S., Kusumoto, S., & Satake, K. 2014. Traveltime delay and initial phase reversal of distant tsunamis coupled with the self-gravitating elastic Earth. J Geophys Res. 119(5):4287-310. http://dx.doi.org/10.1002/2013JB010841.

Wessel, P., & Smith, W.H.F. 1998. New, improved version of Generic Mapping Tools released. Eos Trans AGU. 79(47):579. http://dx.doi.org/10.1029/98EO00426.